Generic Dynamically Reconfigurable Battery With Integrated Auxiliary Output and Balancing Capability

Nima Tashakor, *Member, IEEE*, Jan Kacetl, *Student Member, IEEE*, Jingyang Fang, *Member, IEEE*, Zhongxi Li, *Member, IEEE*, and Stefan Goetz, *Member, IEEE*

***Abstract*—Modular multilevel converters and cascaded H-bridge converters are established concepts in ultrahigh-voltage systems. In combination with batteries, these circuits allow dynamically changing the series/parallel configuration of the battery modules, also known as reconfigurable batteries. A large body of research discusses applications of such systems in grid-storage and electromobility with a single load, such as an electric drive. However, most studies neglect the presence of auxiliary loads, which require additional voltage levels and isolation from the high-voltage battery. This article proposes a decoupling method that can fork a second (galvanically isolated) output off a reconfigurable dc battery without negatively affecting the main output by exploiting the many control degrees of freedom in the modular circuit. The proposed system provides a nonisolated port for the dc link of the motor-drive inverter(s), while generating an additional isolated output at another voltage for auxiliaries. The auxiliary output benefits from the interleaving effect, which increases the operating frequency of the transformer and reduces the filter size. The solution does not require additional active switches for the auxiliary port and can operate with a wide range of voltages. The integrated auxiliary circuit can also balance the modules during idling and charge/discharge cycles. Both simulation and experiments validate the analysis.**

***Index Terms*—Electric vehicles, modular battery-integrated converters, modular multilevel converter, modular reconfigurable battery, multiport converters, split batteries.**

I. Introduction

ALTHOUGH recent technological developments, as well as environmental incentives, have sped up the electric vehicle's expansion into the market, many of the traditional challenges remain. In recent years, a combination of technological progress and request for larger ranges by drivers have almost tripled the capacity of the battery packs used in modern electric vehicles (EVs) [1]. Today, an EV is powered by a mixed serial and parallel connection of literally hundreds of cells. In addition to the increased capacity, a trend toward higher voltage levels is observed that leads to an increasing share of serial connections in batteries with the same energy capacity. Jung discusses the advantages of a higher voltage battery pack (i.e., 800 V) including lower weight, better efficiency, and faster charging [2]. However, higher numbers of serial connections also introduce problems including more complex monitoring, increased loss in balancing, the need for several voltage levels for legacy systems, or safety issues. Another major problem for such systems is the lower efficiency of the inverters at partial load. Longer strings also increase the odds of including cells with below-average performance in the pack due to manufacturing tolerances, which limits the entire pack [3], [4], [5].

Fig. 1(a) depicts the electrical circuit of a conventional EV. The high-power drive system includes high-voltage batteries and often a dc/dc converter that supplies the dc link of the main inverter(s) [6], [7]. In addition, a second low-voltage isolated output supplies the auxiliaries (e.g., lights and control units, and other peripherals). As many studies show, it is possible to further shift the operating point of the inverters by actively regulating the dc-link voltage [8], [9], [10], [11]. Regulating the dc-link voltage improves the efficiency of the system, but the other problems including the balancing battery cells as well as fault tolerance persist [12], [13].

Recent advancements in the field of modular systems and the performance gains of low-voltage transistors have stimulated the development of concepts for dynamically reconfigurable battery systems. Such systems are also called modular battery-integrated converters, split battery systems, or smart batteries [14], [15], [16], [17], [18]. These systems break the previously hard-wired battery pack, which was limited by its weakest element, into subunits and add electronic switches to enable a circuit reconfiguration. The modules have often below 100 V or 60 V (safety extra-low voltage, SELV), and are rarely single-cell modules. Simplified derivates of such concepts are under series development in the vehicle industry [19], [20], [21], [22], [23], [24], [25], [26].

A reconfigurable battery can provide balancing functionality [12], [13], [27], better fault tolerance [28], [29], [30], faster output regulation [31], [32], [33], and increased effective switching frequency resulting in volume reduction [14], [34]. Furthermore, more novel topologies can improve the overall efficiency [35], [36] and provide self-balancing capability [37], [38] as well

Manuscript received 6 October 2022; revised 9 January 2023 and 28 February 2023; accepted 21 March 2023. Date of publication 31 March 2023; date of current version 19 May 2023. This work was supported by the German Research Foundation (Deutsche Forschungsgemeinschaft-DFG) through Grant GO 3306, under Project 470273159. Recommended for publication by Associate Editor F. Gao. *(Corresponding author: Nima Tashakor.)*

Nima Tashakor, Zhongxi Li, and Stefan Goetz are with the Department of Electrical and Computer Engineering, Duke University, Durham, NC 27708 USA (e-mail: nima.tashakor@duke.edu; zhongxi.li@duke.edu; stefan.goetz@duke.edu).

Jingyang Fang is with the School of Control Science and Engineering, Shandong University, Jinan 250100, China (e-mail: jingyangfang@sdu.edu.cn).

Jan Kacetl is with the RPTU Kaiserslautern, Gottlieb-Daimler-Straße, 67663 Kaiserslautern, Germany (e-mail: jkacetl@eit.uni-kl.de).

This article has supplementary material provided by the authors and color versions of one or more figures available at https://doi.org/10.1109/TPEL.2023.3263809.

Digital Object Identifier 10.1109/TPEL.2023.3263809

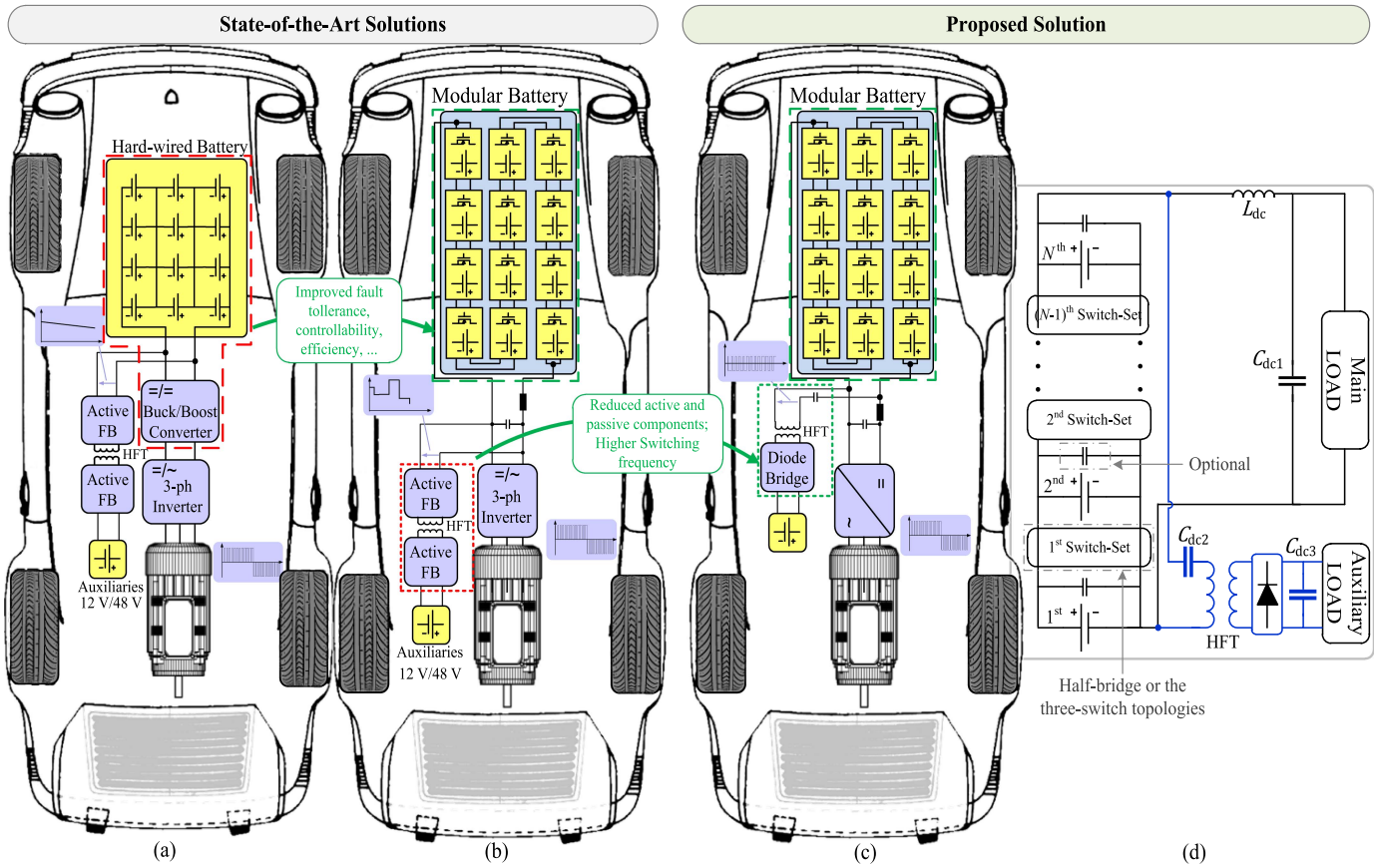

Fig. 1. (a) Conventional electric drive. (b) State-of-the-art electric drive with modular batteries. (c) Proposed electric drive system. (d) Generic electrical circuit of the proposed system.

as bidirectional operation of the modules [39]. Finally, the reconfigurable batteries can reduce the dependency on the weakest cell by creating smaller strings, which in effect results in significant improvement in the capacity [40].

Reconfigurable batteries have been suggested previously. For example, Ma et al. [41], [42] presented a double-arm modular multilevel converter (MMC) topology with batteries for a three-phase energy storage system, but the double-arm topology is more appropriate for capacitor-based MMCs or when modulation of ac and dc is necessary. Gan et al. [14] proposed a battery-integrated MMC for the battery system to provide a fault-tolerant, highly modular, and fully controllable dc-link voltage for driving a switched reluctance motor (SRM). A more detailed review is provided in Part II of the online supplement.

While many different topologies have been proposed for driving the motors, most of the modular topologies ignore the auxiliary load requirements of an EV. Therefore, as Fig. 1(b) depicts, they need a separate isolated dc–dc converter for the low-voltage batteries. Furthermore, due to current safety requirements, auxiliary supplies below the safety extra-low voltage level must be isolated from the high voltage. Isolating the auxiliary unit from the high-voltage battery pack increases the cost, complexity, and volume/weight of the system [43], [44]. To solve the problem of galvanic isolation, Kandasamy et al. [45] proposed an inductively coupled battery-integrated full-bridge inverter. However, multiple high-frequency transformers as well as a high number of active components reduce the efficiency and increase the cost as well as the size of the system. Rehman et al. [46] presented an interesting approach where each battery module exchanges energy with the auxiliaries through an isolated dual-active bridge converter, [47]. Although this approach can offer more flexibility, the cost and complexity of the proposed solution are high. Another possibility is cascaded full-bridge converters as Li et al. proposed in [48], but similar to previous works, a separate isolated converter is necessary. Pinto et al. [43] integrated a part of the auxiliary circuit with the onboard charger to reduce the cost, but a nonmodular battery pack is considered.

Although multiport systems are not a new concept in grid-storage applications, most of the available topologies are not fit for reconfigurable battery systems in EVs [49], [50]. This article fills this gap by presenting a new strategy for a dynamically reconfigurable battery that can greatly simplify the generation of an isolated auxiliary load without a negative impact on the operation of the modular reconfigurable batteries.

The proposed method uses the pulsating dc voltage of the modular battery pack to generate an extra isolated dc voltage for the low-voltage auxiliaries. We provide a generic procedure to decouple the control of the main output and the isolated auxiliaries with minimum interference with other functions. The main dc output can closely follow the optimal operating point of the inverters, while the auxiliary output can achieve a constant voltage and/or controlled current under varying loads. Fewer

semiconductors compared to conventional topologies as well as greatly reduced filter and transformer size further contribute to the appeal of this system. Additionally, the proposed system is capable of sensorless self-balancing by loading some modules more than others.

The rest of this article is organized as follows. The topology and analysis for the dual-port system is presented in Section II. Section III describes the decoupling control strategy for the main as well as auxiliary ports, and Section IV provides simulation as well as experimental results as well as a comparison to the state of the art. Finally, Section V concludes this article.

II. Analysis of the Proposed Dual-Port Reconfigurable Battery

Reconfigurable batteries are an interesting concept that can offer many advantages [12], [13], [27], [51], [52], [53]. Various string connections can provide dc, single-phase, and multiphase structures with specific features [15], [16]. Fig. 1(b) shows the conventional macrostructure of the system considered in the literature. The modular topology in combination with the inductor (L) and the dc capacitor (C_{dc1}) forms a dc–dc buck converter (i.e., circuit in black) that can control the dc-link voltage of the traction inverters. Additionally, an isolated dual-active-bridge converter provides a secondary output for the auxiliaries. However, including a completely separate converter, with many active switches is not cost-effective. Additionally, the switches on the battery side bear the total voltage of the pack (800 V to 1000 V), which makes high switching frequencies challenging and can further increase the size of the transformer (HFT).

As a smarter alternative, this article develops a decoupling technique to simplify and improve the auxiliary circuit using the higher degrees of freedom offered by the modular batteries. Fig. 1(c) illustrates the macrotopology of the proposed system, where the dc capacitors (C_{dc2} and C_{dc3}), the high-frequency transformer, and the diode bridge form a second isolated output port for the auxiliary loads of the EV (the circuit in blue). Comparing Fig. 1(b) and (c) shows that the proposed system requires only a diode bridge with the rated voltage of auxiliaries and the only high-voltage component is a small decoupling capacitor. Additionally, the effective switching frequency is considerably higher, which reduces the volume and size of the transformer as well as the filters. Fig. 1(d) depicts the electrical circuit of the proposed system. As the energy flow is usually from the high-voltage batteries to the auxiliaries, the use of a diode bridge simplifies the controller and reduces the cost of the system. As the size of the storage in the auxiliary unit is negligible and additional functional safety would be necessary, a bidirectional operation would not offer any practical advantage in an EV.

Different topologies can serve as switch-set for battery modules, where half-bridges have the simplest form that can provide a multilevel output voltage using low-voltage switches [52], [54], [55]. However, other topologies such as the three-switch and dual HB topologies provide additional parallel connectivity across modules [53], [56], [57], [58]. As Fig. 2 demonstrates, multiple module topologies apply to the switch sets in Fig. 1(d).

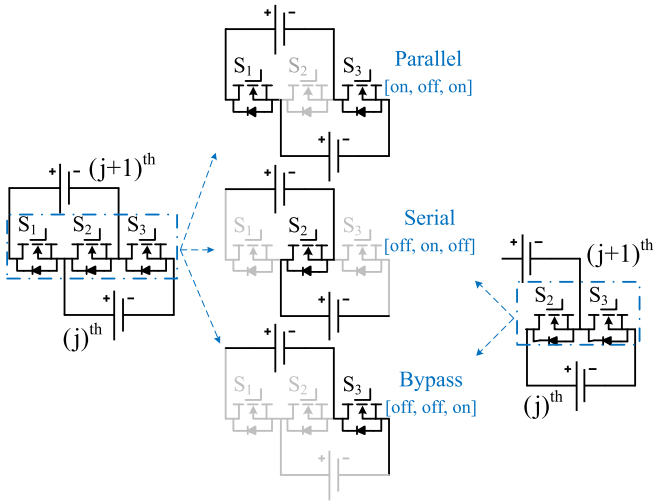

Fig. 2. Simplest forms of module topology with possible operation modes.

Any other module topology that can offer two-level output for the modules is also applicable.

Since the only actively controllable part of the system is the battery modules, conventional control methods cannot regulate both outputs independently. To develop the method for decoupling the control of the two outputs, it is necessary to study the behavior of each converter and derive the equations governing their interactions.

A. High-Power Modular DC–DC Converter

As Fig. 1(a) and (b) illustrates, the state-of-the-art dynamically reconfigurable battery replaces the previously hard-wired battery as well as the separate nonisolated dc–dc converter, while the topology of the auxiliary remains similar. During discharge, it behaves as a multilevel buck converter, which is responsible for maintaining the dc-link voltage of the traction inverters within the optimal range [59], [60]. Determining the optimum operating region of the inverter or the control of the inverter is an established process and outside the focus of this article [59], [61], [62], [63]. Hence, without loss of generality, we consider the desired dc-link voltage as an arbitrary reference value and model the inverter as a variable load connected to it.

The well-known phase-shifted carrier (PSC) modulation generates the switching signals for the modules in the string [39], [64]. Each switch set in Fig. 1(d) corresponds to one carrier. Therefore, N battery modules in Fig. 2 require $(N-1)$ carriers and $(N-1)$ switch sets. The carrier waveforms are compared with one universal modulation index to generate the switching pulses for its respective switch set. Fig. 3 shows an intuitive representation of a system with $(N-1)$ carriers. As Fig. 3 depicts, the effective switching frequency of the system is $(N-1)$ times the frequency of one carrier. Therefore, the dc-link voltage of the main load is

$$V_{\mathrm{dc1}} = (1 + m\,(N-1))\,V_{\mathrm{m}} \tag{1}$$

where V_{m} is the voltage of one module.

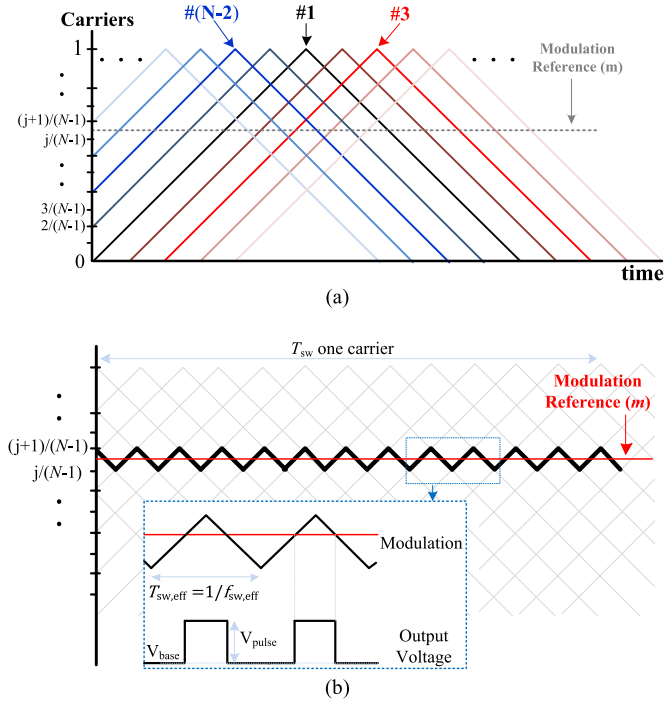

Fig. 3. Intuitive representation of PSC modulation. (a) PSC carriers. (b) Equivalent carriers in the case of symmetrical PSC.

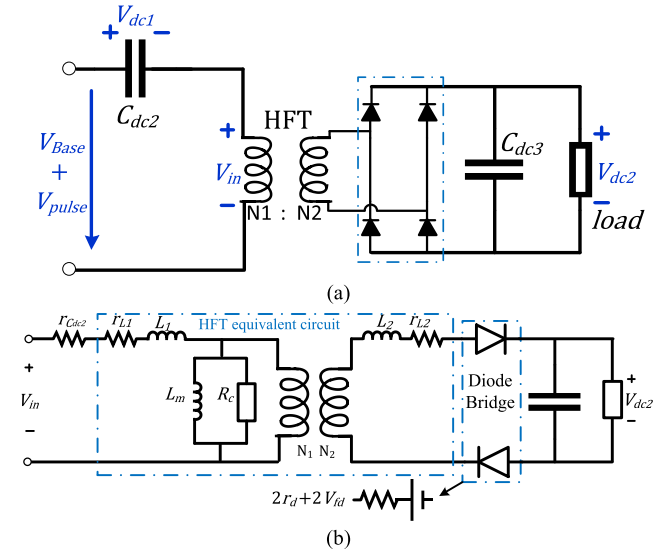

Fig. 4. (a) Circuit diagram of the auxiliary unit. (b) Equivalent electrical circuit with a positive V_{in}.

B. Auxiliary Power Unit

This section derives the necessary equations to estimate the output of the isolated auxiliary port with respect to the modulation index m. Fig. 4(a) shows the circuit of this port, where the input voltage to the circuit is the pulsating output of the reconfigurable pack. Depending on the value of m and N, the output of the system with PSC modulation is similar to the summation of one constant voltage (V_{base}) and a PWM-controlled voltage ($V_{\text{pulse}} \in [V_{\text{m}}, 0]$). As Fig. 3(b) shows, the effective switching

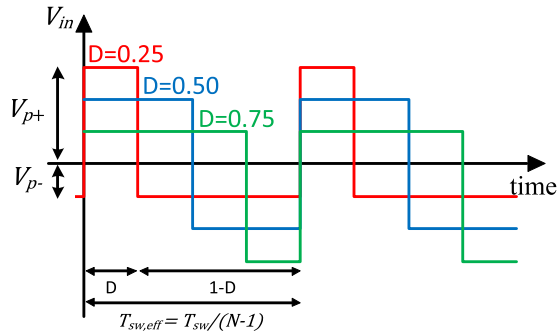

Fig. 5. Intuitive representation of V_{in} with different D.

rate of the pulsating voltage is $(N-1)f_{\text{sw}}$, where f_{sw} is the frequency of one carrier. The value of the base voltage can be calculated using

$$V_{\text{base}} = \lfloor m\,(N-1)+1 \rfloor V_{\text{m}}. \tag{2}$$

Fig. 3(b) shows the effective carrier waveform for the PWM voltage in an intuitive manner. By comparing the modulation reference with the effective carrier waveform, the duty cycle of the pulses follows:

$$D = m\,(N-1) - \text{floor}\,(m\,(N-1)) \tag{3}$$

which indicates a repeating sequence with respect to m.

At each operating point, capacitor C_{dc2} is charged up to V_{dc1} per (1), and the waveform of input voltage (V_{in}) to the switching transformer includes a positive pulse (V_{p+}) and a negative pulse (V_{p-}), which are calculated per

$$V_{p+} = (1-D)\,(V_{\text{m}} - \Delta V_{\text{r}}) \tag{4}$$

$$V_{p-} = -D\,(V_{\text{m}} - \Delta V_{\text{r}}) \tag{5}$$

where ΔV_{r} is the voltage ripple on the capacitor. Varying m changes the value of D, which in turn affects the shape of the input voltage of the transformer. Hence knowing (3), we can control both the width and amplitude of positive and negative pulses through m. Therefore, contrary to the dual-active-bridge topology, both the amplitude and width of the resulting pulses vary with respect to m and consequently D. Fig. 5 displays this variation intuitively. According to (4) and (5), increasing D increases the width of V_{p+} but also in effect reduces its amplitude and vice versa. Two situations are possible depending on D per

$$\begin{cases} D \le 0.5 \\ D > 0.5 \end{cases} \Rightarrow \begin{matrix} V_{p+} \ge V_{p-} \\ V_{p+} < V_{p-} \end{matrix} . \tag{6}$$

For $D < 0.5$, the positive pulse is larger. Hence, during $0 \le t \le DT_{\text{sw,eff}}$, the diode bridge is forward-biased, and the capacitor (C_{dc3}) is charged. During $DT_{\text{sw,eff}} \le t \le T_{\text{sw,eff}}$ interval with $V_{p-} < V_{\text{dc2}}$, the diode bridge is reverse-biased, and C_{dc3} discharges into the load. The output of the system for $D < 0.5$ follows:

$$V_{\text{dc2}} = (V_{p+})\,\frac{N_2}{N_1} \tag{7}$$

where $\frac{N_2}{N_1}$ is the transformer ratio.

Finally, the ideal gain of the system for $D \leq 0.5$ is

$$\frac{V_{\text{dc2}}}{V_{\text{m}}} = \left(\frac{1-D}{1+\frac{\Delta V_{\text{r}}}{V_{\text{m}}}}\right)\frac{N_2}{N_1}. \tag{8}$$

Considering the voltage drop across the parasitic or stray elements of the auxiliary path shown in Fig. 4(b), a more realistic gain for $D \leq 0.5$ can be derived that follows:

$$\frac{V_{\text{dc2}}}{V_{\text{m}}} = \frac{(1-D)\frac{N_2}{N_1}\left(1-\frac{\Delta V_{\text{r}}}{V_{\text{m}}}\right)-\frac{2V_{\text{fd}}}{V_{\text{m}}}}{R_{\text{eq}}+1}. \tag{9}$$

The complete derivation process is provided as an online supplement.

Equation (9) can be further simplified by neglecting V_{fd} and ΔV_{r} into

$$\frac{V_{\text{dc2}}}{V_{\text{m}}} = \left(\frac{1-D}{R_{\text{eq}}+1}\right)\frac{N_2}{N_1}. \tag{10}$$

Value of R_{eq} in (9) and (10) is the equivalent resistance of the system that can be written as

$$R_{\text{eq}} = \left(\left(\frac{N_2}{N_1}\right)^2\left(r_{C_{\text{dc2}}}+r_{L1}\right)+r_{L2}+2r_{\text{fd}}\right)\frac{1}{D\cdot R_{\text{load}}} \tag{11}$$

For D $>$ 0.5, the negative pulse is larger. Therefore, the diode bridge is reverse-biased during positive pulses ($0 \leq t \leq DT_{\text{sw,eff}}$), and the capacitor charges during the negative pulses ($DT_{\text{sw,eff}} \leq t \leq T_{\text{sw,eff}}$). The output of the system for $D > 0.5$ follows:

$$V_{\text{dc2}} = (V_{p-})\frac{N_2}{N_1}. \tag{12}$$

Finally, the ideal gain of the system for $D > 0.5$ is

$$\frac{V_{\text{dc2}}}{V_{\text{m}}} = \left(\frac{D}{1+\frac{\Delta V_{\text{r}}}{V_{\text{m}}}}\right)\frac{N_2}{N_1}. \tag{13}$$

Considering the components representing parasitics, as shown in Fig. 4(b), a more realistic gain for $D > 0.5$ can be derived per

$$\frac{V_{\text{dc2}}}{V_{\text{m}}} = \frac{D\frac{N_2}{N_1}\left(1-\frac{\Delta V_{\text{r}}}{V_{\text{m}}}\right)-\frac{2V_{\text{fd}}}{V_{\text{m}}}}{R_{\text{eq}}+1}. \tag{14}$$

By neglecting V_{fd} and ΔV_{r}, (14) is simplified to

$$\frac{V_{\text{dc2}}}{V_{\text{m}}} = \left(\frac{D}{R_{\text{eq}}+1}\right)\frac{N_2}{N_1} \tag{15}$$

where R_{eq} in (14) and (15) is the equivalent resistance of the system that can be written as

$$R_{\text{eq}} = \left(\left(\frac{N_2}{N_1}\right)^2 r_{\text{eq1}}+r_{\text{eq2}}\right)\frac{1}{(1-D)R_{\text{load}}}. \tag{16}$$

Comparing (10) and (15) shows a symmetry between the two relations with respect to $D = 0.5$. The gains of the system for $D = 0.25$ and $D = 0.75$, for example, are similar. It is possible to write both equations as

$$\frac{V_{\text{dc2}}}{V_{\text{m}}} = \frac{\max(D,\,1-D)}{R_{\text{eq}}+1}. \tag{17}$$

Due to the symmetry as Fig. 7 illustrates, there are two possible D values for each operating point of V_{dc2}. Furthermore, based on (3), each value of D entails $(N-1)$ possible values for m. Therefore, there are $2(N-1)$ values for m at each operating point that lead to an identical voltage in the output of the auxiliary power unit (V_{dc2}) but a completely different output in the dc-link voltage (V_{dc1}). In other words, there are $2(N-1)$ possible V_{dc1} values for each operating point of the auxiliary load (i.e., for a specific D). The possible values of m that result in similar D follow:

$$m_i(D) = \left(\frac{i-1+D}{N-1}\right),\left(\frac{i-D}{N-1}\right)\ \forall\, i = 1,\ldots,N-1 \tag{18}$$

and consequently, possible V_{dc1} values are

$$V_{\text{dc1},i} = ((N-1)\,m_i(D)+1)\,V_{\text{m}}. \tag{19}$$

III. Proposed Controller and System Design

The main objective of the system is to follow the reference voltage of the main load as closely as possible, while providing a constant voltage to the auxiliaries. Based on the analysis in Section II, there are $2(N-1)$ operating points for the dc-link voltage for each operating point of the auxiliary output. The extra degrees of freedom offered by the circuit can be exploited to develop a controller that can individually control the output of each load. In doing so, first the controller determines the suitable operating point for the auxiliary load (D^*), and then calculates the best m among the $2(N-1)$ candidates. Due to nonideal components, a closed loop controller regulates the operating point of the auxiliary through D.

A. Generic Control Algorithm With Both Ports Active

The optimum operating dc-link voltage for inverter ($V_{\text{dc1}}^{\text{ref}}$) is arbitrary within the complete voltage range of the batteries and is considered as an input from the higher-level control loops. The output voltage of auxiliary power unit (V_{dc2}) is constant (e.g., in most EVs either around 12 V per LV 124 standard or 48 V per LV 148 and VDA 320 standards).

Fig. 6 provides the proposed control algorithm for the dual port system. At each instance, the reference values for V_{dc1} are provided by the efficiency maps of the system. The value of $V_{\text{dc2}}^{\text{ref}}$ is the rated voltage of the auxiliary power unit. V_{dc2} is the measured voltage at the output of the auxiliary power unit and $\overline{V_{\text{m}}}$ is the average operating voltage of the modules. First, a PI controller determines the required D^* to maintain the voltage of the auxiliary output constant. Then, the algorithm determines the possible modulation indices (m_i) according to (18) for D^* and $(1-D^*)$ and select the one that minimizes the difference between V_{dc1} and $V_{\text{dc1}}^{\text{ref}}$ according to (19). Hence, the output voltage of the auxiliary unit is fully controlled, and the dc-link voltage of the inverters is maintained within a small boundary of the optimal point.

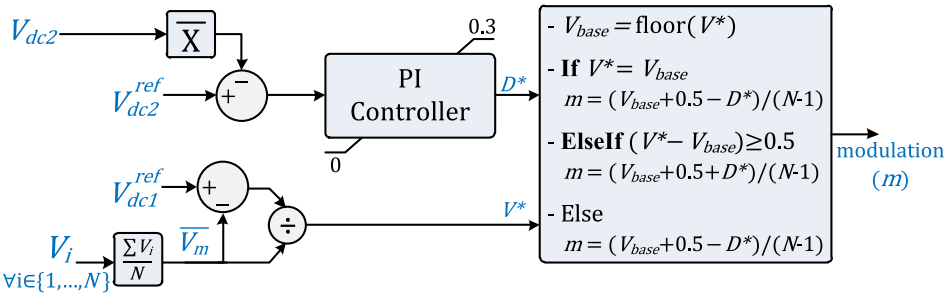

Fig. 6. Proposed control algorithm for the dual-port system.

Based on the number of the modules and the transformer ratio, the maximum deviation of the dc-link voltage from $V_{\mathrm{dc1}}^{\mathrm{ref}}$ is

$$\Delta V_{\max} \leq \frac{0.5}{1-N} V_{\mathrm{m}}. \tag{20}$$

Additionally, a hysteresis block in the input of the PI controller reduces fluctuations.

B. Self-Balancing Capability

For $D \leq 0.5$, the diode bridge only conducts during the positive pulses, and the higher the amplitude of a positive pulse is, the higher would be the energy transfer during that interval. As long as all the modules are at similar voltages, then similar amounts of charge are drawn from each module. However, if a module has a higher voltage, it will increase the amplitude of its corresponding positive pulses and leads to higher charge transfers in those intervals. Consequently, the auxiliary circuit draws more energy from modules with higher voltages at higher state-of-charges (SOCs) and lower energy from modules with lower voltages at lower SOCs.

The balancing rate quadratically depends on the voltage difference of the modules from the average module voltage ($\bar{V}_m$) following:

$$\Delta E_{B_j} \propto \left(V_{\mathrm{m}_j}^2 - \bar{V}_{\mathrm{m}}^2\right) \tag{21}$$

where ΔE_{B_j} and V_{m_j} are, respectively, the energy difference and the terminal voltage of the jth module. Therefore, modules with above-average terminal voltage are discharged more, and modules with below-average voltage are discharged less.

This effect forms an inherent voltage balancing capability independent of the module topology and without any additional controller. The relationship between SoC and voltage may not be consistent in highly degraded batteries. However, balancing efforts can be further adjusted using conventional techniques, such as cell sorting or droop control [65], [66].The balancing effect is particularly of use during idling conditions, where no current is drawn from the main port, but the auxiliary unit is still operating. In this case, we can use the integrated auxiliary unit to provide power and at the same time, balance the modules. In such cases, it is recommended to minimize the modulation index of the modules to reduce the stress on the dc-link as well as the decoupling capacitors. Therefore, to obtain the control algorithm in this mode, it suffices to set $V_{\mathrm{dc1}}^{\mathrm{ref}}$ in Fig. 6 to a minimum.

TABLE I
PARAMETERS OF THE SIMULATED SYSTEM

PARAMETER	VALUE
V_{dc1}	400 V – 800 V
C_{dc1}	20 µF
L_{dc}	23 µH
C_{dc2}	348 µF
C_{dc3}	5.4 mF
R_{ldc}	10 mΩ
$P_{\mathrm{load,1}}$	300 kW
$P_{\mathrm{load,2}}$	5 kW
f_{carrier}	5 kHz
$f_{\mathrm{sw,effective}}$	25 kHz
R_{ds}, R_{d}	1 mΩ
V_{m}	82 V – 103 V
$r_{\mathrm{bt,1\sim8}}$	5 mΩ

C. Design Considerations

The L_{dc} and C_{dc1} can be selected rather conventionally as the general behavior of the main port is similar to a buck converter with much higher effective switching frequency [67].

The values of module voltage and the expected voltage of the auxiliary power unit dictate the transformer ratio N_2:N_1. Based on (10) and (15) the suitable range of N_2:N_1 is

$$\frac{(R_{\mathrm{eq}}+1)\,(V_{\mathrm{dc2}}-V_{\mathrm{fd}})}{0.95(V_{\mathrm{m}}-\Delta V_{\mathrm{r}})} \leq \frac{N_2}{N_1} \leq \frac{(R_{\mathrm{eq}}+1)\,(V_{\mathrm{dc2}}-V_{\mathrm{fd}})}{0.5(V_{\mathrm{m}}-\Delta V_{\mathrm{r}})}. \tag{22}$$

Although in theory (22) shows a large range to calculate the transformer ratio since the voltage of the battery modules can vary according to their state of health (e.g., for many Li-Ion cell chemistries $0.8\ V_{\mathrm{rated}} \leq V_{\mathrm{m}} \leq 1.2\ V_{\mathrm{rated}}$, such as Li-NMC), a more practical relation is

$$\frac{(R_{\mathrm{eq}}+1)\,(V_{\mathrm{dc2}}-V_{\mathrm{fd}})}{0.95(V_{\mathrm{m,min}}-\Delta V_{\mathrm{r}})} \leq \frac{N_2}{N_1} \leq \frac{(R_{\mathrm{eq}}+1)\,(V_{\mathrm{dc2}}-V_{\mathrm{fd}})}{0.5(V_{\mathrm{m,max}}-\Delta V_{\mathrm{r}})} \tag{23}$$

where $V_{\mathrm{m,min}}$ and $V_{\mathrm{m,max}}$ are the minimum and maximum operating voltages of one module.

Furthermore, due to R_{eq} in (11) and (16), the gain of the system is not completely linear. As D goes to the upper and lower bounds (i.e., close to one and zero), the effect of parasitic impedance on the system increases linearly. As an example, Fig. 7 compares the achieved gains through simulations with the

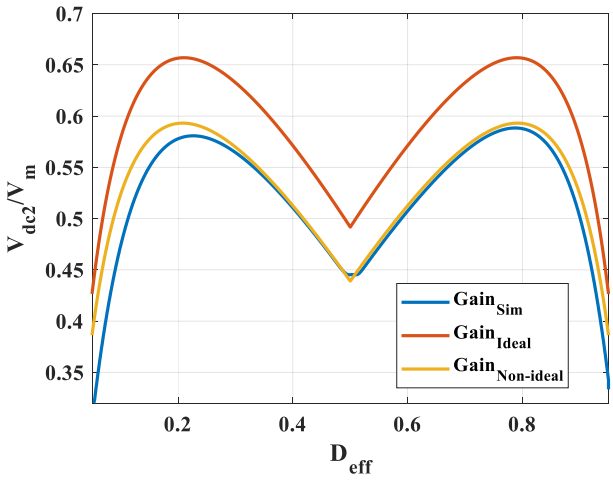

Fig. 7. Gain variations of the auxiliary power unit with respect to D.

ideal as well as nonideal relations. Table I shows the parameters of the simulated setup.

Based on Fig. 7, designing the normal operating point of the system close to $D = 0.5$ improves the controllable range of the system, and $D < 0.2$ or $D > 0.8$ deteriorates the system performance. Therefore, the upper boundary of N_2:N_1 in (23) is the optimal value. Replacing R_{eq} with (11) or (16) and solving for N_2:N_1 gives the suitable value for the transformer ratio.

Capacitor C_{dc2} is responsible for decoupling the dc and switching components of the voltage. According to (9) and (14), the voltage ripple of capacitor C_{dc2} can significantly affect the system's behavior. Using an analysis similar to the design of the transformer ratio, the minimum capacitor for the system is

$$C_{\text{dc2}} = \frac{P_{\text{max2}}}{V_{\text{dc2}} \Delta V_{\text{r}} \underbrace{f_{\text{sw,effective}}}_{(N-1) f_{\text{sw}}}} \frac{N_2}{N_1} \tag{24}$$

where P_{max2} is the maximum output power of the auxiliary unit, and $f_{\text{sw,effective}}$ is the effective switching frequency. Similarly, the minimum capacitance of capacitor C_{dc3} is

$$C_{\text{dc3}} = \frac{P_{\text{max2}}}{V_2 \Delta V_{\text{r}} f_{\text{sw,effective}}}. \tag{25}$$

As the reconfigurable battery increases the effective frequency and reduces the voltage steps, compared to a conventional battery pack, the required capacitances (C_{dc1}, C_{dc2}, and C_{dc3}) and the inductance (L_{dc}) are reduced by a factor of $^1/_{(N-1)}$.

The LC network (L_1 and C_{dc1}) in the system with a resistive load form a parallel RLC network with the characteristic equation of

$$S^2 + \left(\frac{R_{\text{eq}}}{L_{\text{dc}}} + \frac{1}{R_{\text{load}} C_{\text{dc1}}}\right) S + \left(\frac{R_{\text{eqs}}}{R_{\text{load}}} + 1\right) \left(\frac{1}{L_{\text{dc}} C_{\text{dc1}}}\right) = 0 \tag{26}$$

where R_{eq} is the equivalent resistance of all components in series with the inductor. Due to the small size of the inductor, i.e., $L_{\text{dc}} \ll 4R_{\text{load}}^2 C_{\text{dc1}}$), (26) is typically an underdamped system with the damping coefficient $\alpha = \frac{1}{2}(\frac{1}{R_{\text{load}} C_{\text{dc1}}} + \frac{R_{\text{eq}}}{L_{\text{dc}}})$, and the natural frequency is approximately $\omega_n = \sqrt{(\frac{1}{L_{\text{dc}} C_{\text{dc1}}})}$.

The resulting transfer function of the system with a PI controller neglecting the feedforwards is

$$H(s) = \frac{V_{\text{ref1}}}{V_{\text{dc1}}} = \frac{\frac{k_{\text{p1}}(N-1)V_{\text{m}}}{L_{\text{dc}} C_{\text{dc1}}} S + \frac{k_{\text{i1}}(N-1)V_{\text{m}}}{L_{\text{dc}} C_{\text{dc1}}}}{S^3 + 2\alpha S^2 + \omega_n^2 S} \tag{27}$$

where k_{p1} and k_{i1} are the PI coefficients. The system with resistive load is fully stable with resistive loads. Similarly, the dynamic response of the auxiliary port can also be investigated.

D. Comparison With State of the Art

The proposed system has all the general advantages contributed to a modular battery system, regardless of the integrated auxiliary port [14], [16], [35], [45], [51], [68], [69], [70]. Additionally, the proposed system has a lower number of semiconductors compared to other modular multilevel batteries with independent auxiliary circuit [14], [15], [16], [71]. The transformer for the auxiliary unit operates at a lower voltage and with $(N-1)$-times the switching frequency of one module, which reduces its volume and weight considerably. Similarly, the passive components in the auxiliary port are significantly smaller due to the benefit of higher frequency as well as better voltage quantization. Furthermore, almost all components in the auxiliary port operate at the module voltage level and do need to tolerate the complete voltage of the system. Finally, the sensorless balancing capability can ensure that the battery modules stay balanced during operation even without a closed-loop balancing controller. A detailed comparison of the proposed system with the state of the art is provided in Part II of the online supplement.

IV. Results and Discussion

A. Simulation Results

MATLAB/Simulink serves to simulate a system with ten modules, where Table I provides its main parameters. The modular battery feeds a variable load with a variable reference voltage. The rated voltage of the battery is 91 V, which can fluctuate between 80 V to 105 V. We set $V_{\text{dc2}}^{\text{ref}} = 48$ V, as 48 V supplies are becoming established in many executive and sports cars. Based on the module voltage range as well as $V_{\text{dc2}}^{\text{ref}}$ value, (23) determines the ratio of the transformer to approximately 1.13.

Fig. 8 shows the voltage and current waveforms for the first and second outputs, and Fig. 9 depicts the pulsating output of the reconfigurable battery. During the simulation, the optimal reference voltage and also demand power for the first output as well as the demand power of the second output are varied. The controller can provide a fixed V_{dc2} under stark variations of the operation point of both outputs. Additionally, the voltage of the first output closely follows the optimal value provided as a reference to the controller. The steady-state ripple of V_{dc1} and V_{dc2} is below 3% and 1%, respectively.

Fig. 10 shows the modulation signals as well as the voltage deviation of both outputs from their respective goals. Despite some transients at the beginning of each step, the steady-state

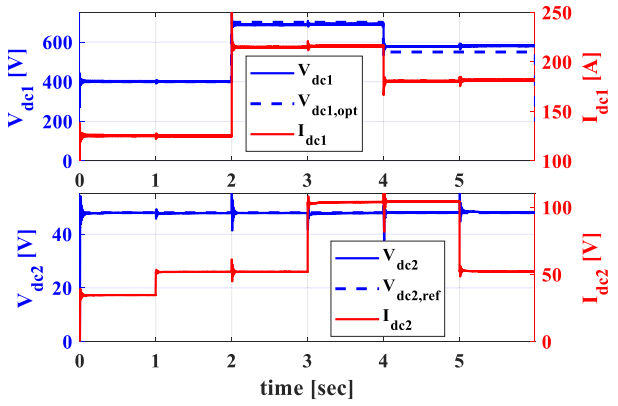

Fig. 8. Voltage and current waveforms for the simulated system.

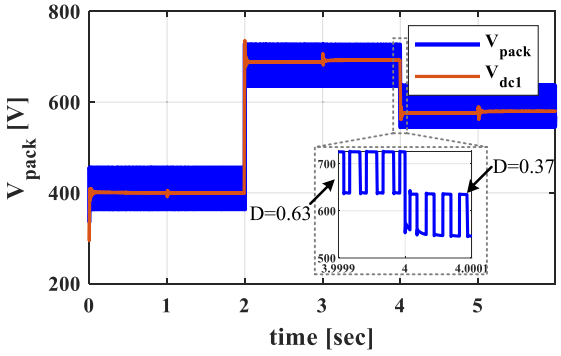

Fig. 9. Pulsating voltage of the modular reconfigurable battery.

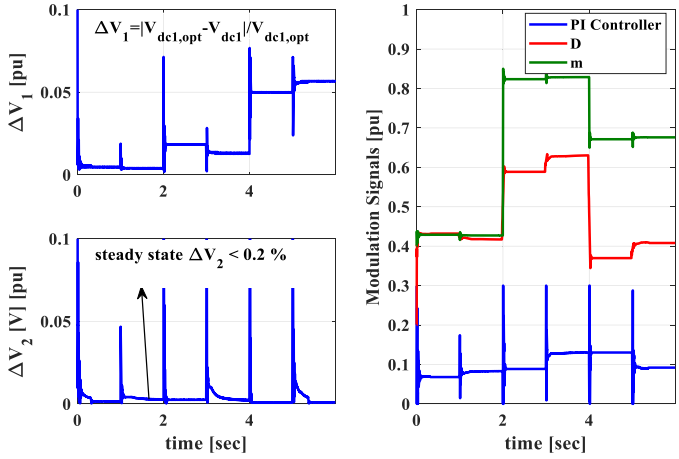

Fig. 10. Control signals as well as the outputs' deviations from reference values.

error for the second output is below 0.2%. Similarly, maximum voltage deviation of V_{dc1} from its optimal value is below 6%.

Additionally, Fig. 11 shows the inherent self-balancing performance of the system with both ports active. In the simulated system, multiple modules have different initial SOC values as well as a maximum 6% capacity tolerance from the rated values. The speed of convergence is initially high but falls as the SOCs converge to the average SOC and the differences between the terminal voltages of the modules reduce. Fig. 11 demonstrates

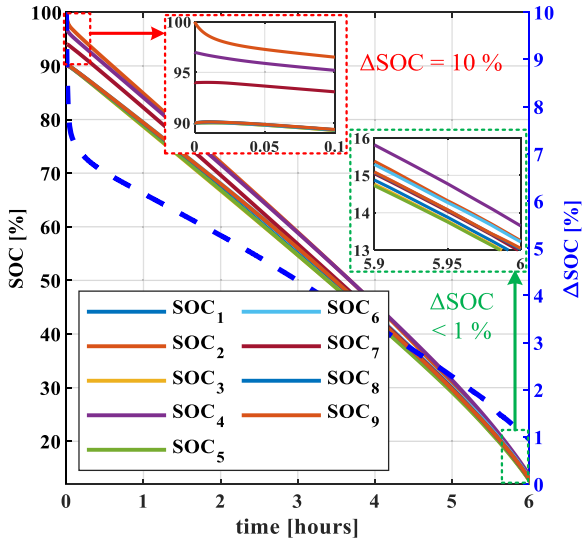

Fig. 11. Balancing performance of the integrated auxiliary when both ports are actively discharging the modules ($P_1 = 25$ kW, $P_2 = 3$ kW).

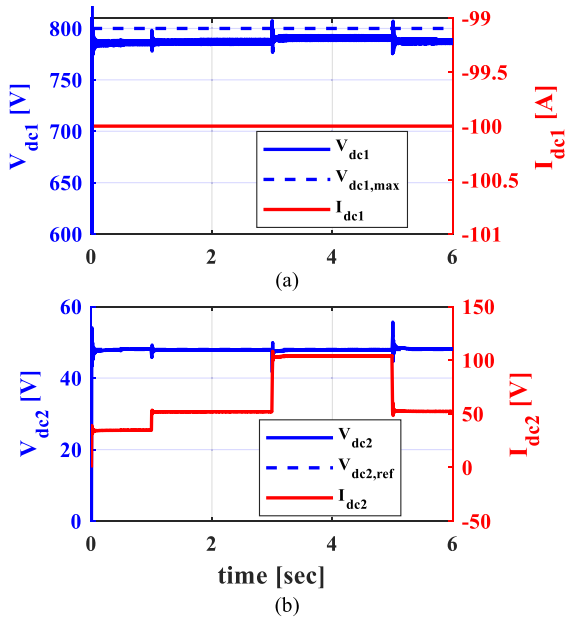

Fig. 12. Voltage and current profiles of the reconfigurable battery ports during charging. (a) Voltage and current of the main port. (b) Voltage and current of the auxiliary port.

that it can balance the modules to below 1% imbalance boundary, which depends on the parasitic voltage drop as well as the capacity tolerances. The additional results are also provided in Part III of the provided online supplement.

Similar to the discharge mode, the proposed system can also supply power to the auxiliaries when the battery pack is charged. Fig. 12 displays the terminal voltage and current of the auxiliary during charging with a constant current of 100 A. The online supplement provides additional results and explanations.

B. Experimental Results

We built two prototype reconfigurable battery packs with five and nine modules. An FPGA-based rapid prototyping controller

TABLE II
PARAMETERS OF THE LABORATORY SETUP

PARAMETER	VALUE
V_{dc1}	20 V – 100 V
C_{dc1}	100 µF
L_{dc}	200 µH
C_{dc2}	940 µF
C_{dc3}	2.7 mF
R_{ldc}	50 mΩ
$P_{load,1}$	2 kW
$P_{load,2}$	36 W
$f_{carrier}$	5 kHz
$f_{sw,effective}$	25 kHz
R_{ds}, R_d	1 mΩ
V_m	22 V – 25.2 V
$r_{bt,1\sim8}$	20 mΩ

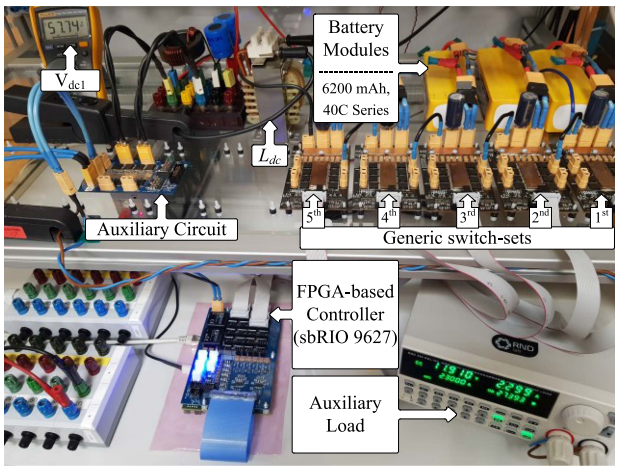

Fig. 13. Laboratory testbench.

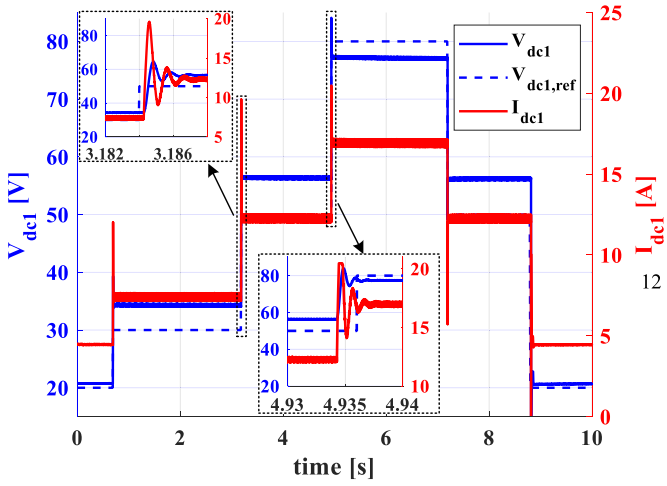

Fig. 14. Measured voltage and currents at the semi-controlled main port.

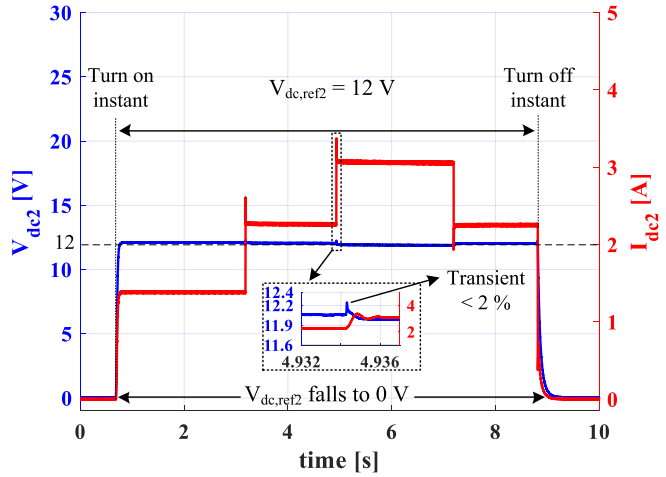

Fig. 15. Measured voltage and currents at the auxiliaries.

(sbRIO 9726) implements the proposed control algorithms as well as the PSC modulation. The measurements are recorded using an eight-channel oscilloscope from LeCroy. An isolated transducer (LV25P due to its low settling time) with an analog amplifier provides the isolated feedback of the second dc output. Each battery module consists of six series cells that provide a 24 V open-circuit voltage. An RL load with a resistance of 5.5 Ω is connected to the first dc output, while a controllable electronic load is connected to the second isolated output. Table II summarizes the parameters of the laboratory setup, and Fig. 13 shows the laboratory testbench.

The desired voltage of the first dc output ($V_{dc1,ref}$) is provided as an adjustable input signal to the controller, while the reference output of the auxiliary port only varies between 0 V when it is turned OFF and 12 V when operating. The controller uses the proposed algorithm to determine the most suitable modulation index and then generates the switch signals for all modules. Fig. 14 shows the measurements for the output voltage and current of the main output port. The value of V_{dc1}closely follows its reference value ($V_{dc1,ref}$) in each step. The voltage ripple at the main output port is below 3%, which is within the design criteria of C_{dc1}. There are small overshoots and undershoots after significant variations in the operating point of the system, but these variations stay below a 10 V and settling time of approximately 0.5 ms. Fig. 15 presents the voltage and current at the terminal of the auxiliaries that shows a zero steady-state error. Similarly, small transients are observed due to the sudden changes in the operating point of the system, but the variations are even less prominent and remain below 0.25 V.

Although the output voltage of the main port is always close to its desired value, it does not fully converge since there are only eight possible points with $N = 5$. However, the number of battery modules is considerably higher, and hence V_{dc1} can even more closely follow the reference. Neglecting minor transients, the output voltage of the auxiliaries fully follows its reference value at all times or irrespective of the number of modules.

Fig. 16 displays the deviations of the output voltages from the reference values. The output voltage of the isolated output (V_{dc2}) stays below the 2% mark. Concurrently, even with relatively large deviations in the reference voltage of the nonisolated output, the provided output voltage is within a 6% boundary, which is a significant improvement compared to conventional systems with a fixed dc-link voltage. Furthermore, Fig. 17 shows

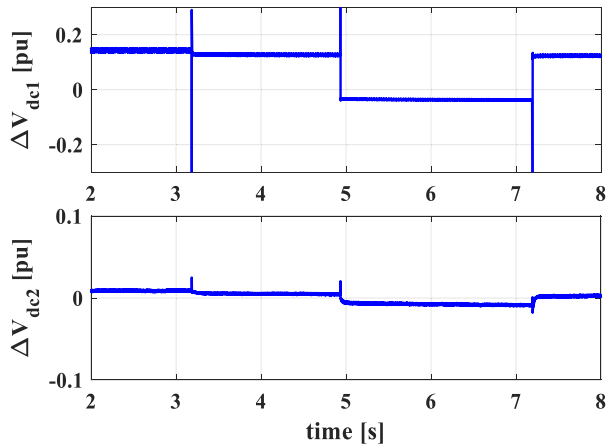

Fig. 16. Voltage deviations from the reference values.

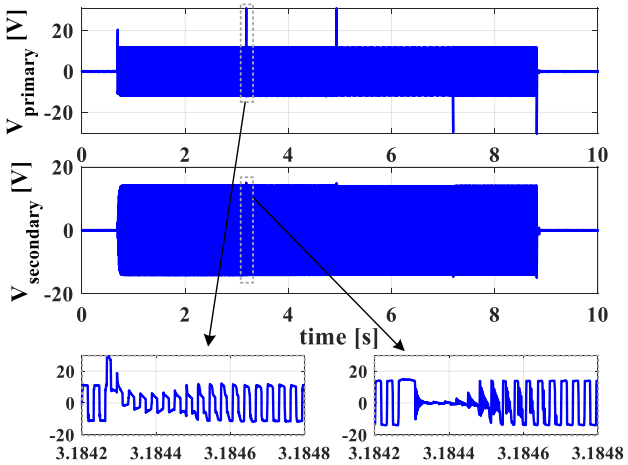

Fig. 17. Primary and secondary voltages of the transformer.

the primary and secondary voltages of the switching transformer, which confirms that the voltage at the primary of the transformer is close to $V_{\mathrm{m}}/2$, regardless of the dc-link voltage at the main port. The limited range of the voltage at the transformer's primary simplifies its isolation requirements. There are small spikes reflecting the transients on the primary side due to sudden changes in the operating point of the reconfigurable battery, but the filtering properties of the HFT eliminate them on the secondary side.

Another advantage of the presented method and topology compared to the more conventional reconfigurable battery system is that the proposed system can fully benefit from the higher equivalent switching frequency of the modular pack as well as the better voltage quantization, reducing the size of the high-frequency transformer. Furthermore, the new auxiliary circuit does not require any high-voltage full-bridge circuit on the battery side, which can considerably reduce cost.

The developed system can be easily extended to a higher number of modules, without any modification in the proposed controller. To verify that, Part V of the online supplement presents a larger setup with nine modules and higher voltage and power ratings. The results verify the improved performance of the system, including higher effective switching frequency, lower ripple, and reduced steady-state error. The larger prototype could achieve an approximately 94.5% to 95.5% efficiency at 5 kW.

V. Conclusion

This article proposes a topology and control method for a modular multilevel battery with an integrated auxiliary circuit for electromobility application. The structure forks off a second (galvanically isolated) dc voltage. In addition, we propose a control technique for both outputs using the extra degrees of freedom inherently available in the reconfigurable battery. The main output supplies the traction system of the electric vehicle, while the lower-power isolated output supplies the auxiliary system.

The provided method allows for considerable simplification of the circuit of the auxiliary output while benefiting from all the advantages of a module battery setup, such as higher effective switching frequency and lower voltage components. For the auxiliaries, no extra active or controlled components are necessary, which further adds to the appeal of this technique. Moreover, the integrated auxiliary output is capable of balancing the modules' voltages by discharging the modules with higher terminal voltage.

The article analyzes the behavior of the system and provides design guidelines for both controller and topology. The provided analysis as well as simulation and real measurements support the applicability and performance of the proposed topology and method. In contrast to $>$ 40% output fluctuations in a conventional hard-wired battery pack, the nonisolated traction output is controlled within 6% of the rated voltage with five modules, which can be further reduced to 3% using nine modules. The resolution of the traction output can be even further improved with a higher number of modules.

While the article mainly focuses on the operation of the system during discharge mode, the same principles are applicable when the battery is charging. The battery modules can be charged with a constant current while the output voltage of the auxiliary unit is controlled using the proposed decoupling control strategy. Nevertheless, a detailed study of the system during charging as and further interactions of the chargers with the modular battery system is interesting and considered a future work.

References

[1] B. Arabsalmanabadi, N. Tashakor, S. Goetz, and K. Al-Haddad, "Li-ion battery models and a simplified online technique to identify parameters of electric equivalent circuit model for EV applications," in *Proc. IEEE 46th Annu. Conf. Ind. Electron. Soc.*, Oct. 18–21, 2020, pp. 4164–4169.

[2] C. Jung, "Power up with 800-V systems: The benefits of upgrading voltage power for battery-electric passenger vehicles," *IEEE Electrific. Mag.*, vol. 5, no. 1, pp. 53–58, 2017, doi: 10.1109/MELE.2016.2644560.

[3] M. Jaensch, J. Kacetl, T. Kacetl, and S. Götz, "Modulation index improvement by intelligent battery," U.S. Patent 10,784,698, Sep. 22, 2020.

[4] Y. Yang, Q. Ye, L. J. Tung, M. Greenleaf, and H. Li, "Integrated size and energy management design of battery storage to enhance grid integration of large-scale PV power plants," *IEEE Trans. Ind. Electron.*, vol. 65, no. 1, pp. 394–402, Jan. 2018.

[5] J. Zhang, Z. Wang, P. Liu, and Z. Zhang, "Energy consumption analysis and prediction of electric vehicles based on real-world driving data," *Appl. Energy*, vol. 275, 2020, Art. no. 115408.

[6] J. Reimers, L. Dorn-Gomba, C. Mak, and A. Emadi, "Automotive traction inverters: Current status and future trends," *IEEE Trans. Veh. Technol.,* vol. 68, no. 4, pp. 3337–3350, Apr. 2019, doi: 10.1109/TVT.2019.2897899.

[7] S. S. Williamson, A. K. Rathore, and F. Musavi, "Industrial electronics for electric transportation: Current state-of-the-art and future challenges," *IEEE Trans. Ind. Electron.,* vol. 62, no. 5, pp. 3021–3032, May 2015, doi: 10.1109/TIE.2015.2409052.

[8] E. P. Wiechmann, P. Aqueveque, R. Burgos, and J. Rodríguez, "On the efficiency of voltage source and current source inverters for high-power drives," *IEEE Trans. Ind. Electron.*, vol. 55, no. 4, pp. 1771–1782, Apr. 2008.

[9] S. Rohner, S. Bernet, M. Hiller, and R. Sommer, "Modulation, losses, and semiconductor requirements of modular multilevel converters," *IEEE Trans. Ind. Electron.*, vol. 57, no. 8, pp. 2633–2642, Aug. 2010, doi: 10.1109/TIE.2009.2031187.

[10] A. K. Sadigh, V. Dargahi, and K. Corzine, "Analytical determination of conduction power loss and investigation of switching power loss for modified flying capacitor multicell converters," *IET Power Electron.*, vol. 9, no. 2, pp. 175–187, 2016.

[11] Z. Li, A. Yang, G. Chen, Z. Zeng, A. V. Peterchev, and S. M. Goetz, "A high-frequency pulsating dc link for electric vehicle drives with reduced losses," in *Proc. IEEE Ind. Electroncis Soc.*, Toronto, Canada, 2021, pp. 1–6.

[12] Y. Zhu, W. Zhang, J. Cheng, and Y. Li, "A novel design of reconfigurable multicell for large-scale battery packs," in *Proc. Int. Conf. Power Syst. Technol.*, Nov. 6–8, 2018.

[13] M. A. Rahman, K. Craemer, J. Büscher, J. Driesen, P. Coenen, and C. Mol, "Comparative analysis of reconfiguration assisted management of battery storage systems," in *Proc. IEEE 45th Annu. Conf. Ind. Electron. Soc.*, Oct. 14–17, 2019, pp. 5921–5926.

[14] C. Gan, Q. Sun, J. Wu, W. Kong, C. Shi, and Y. Hu, "MMC-based SRM drives with decentralized battery energy storage system for hybrid electric vehicles," *IEEE Trans. Power Electron.,* vol. 34, no. 3, pp. 2608–2621, Mar. 2019, doi: 10.1109/TPEL.2018.2846622.

[15] N. Tashakor, E. Farjah, and T. Ghanbari, "A bidirectional battery charger with modular integrated charge equalization circuit," *IEEE Trans. Power Electron.,* vol. 32, no. 3, pp. 2133–2145, Mar. 2017, doi: 10.1109/TPEL.2016.2569541.

[16] Y. Li and Y. Han, "A module-integrated distributed battery energy storage and management system," *IEEE Trans. Power Electron.,* vol. 31, no. 12, pp. 8260–8270, Dec. 2016, doi: 10.1109/TPEL.2016.2517150.

[17] S. M. Goetz, Z. Li, X. Liang, C. Zhang, S. M. Lukic, and A. V. Peterchev, "Control of modular multilevel converter with parallel connectivity—Application to battery systems," *IEEE Trans. Power Electron.*, vol. 32, no. 11, pp. 8381–8392, Nov. 2017.

[18] Z. Zedong, W. Kui, X. Lie, and L. Yongdong, "A hybrid cascaded multilevel converter for battery energy management applied in electric vehicles," *IEEE Trans. Power Electron.*, vol. 29, no. 7, pp. 3537–3546, Jul. 2014, doi: 10.1109/TPEL.2013.2279185.

[19] M. Jaensch, J. Kacetl, T. Kacetl, and S. Götz, "Vehicle having an energy storage element," U.S. Patent 11,088,550, Aug. 10, 2021.

[20] M. Jaensch, J. Kacetl, T. Kacetl, and S. Götz, "DC charging of an intelligent battery," U.S. Patent 11,152,797, Oct. 19, 2021.

[21] J. A. Qahouq, "Distributed battery power electronics architecture and control," U.S. Patent 9,368,991, Jun. 14, 2016.

[22] M. Ishigaki, S. Tomura, T. Umeno, and K. Kimura, "Power conversion circuit and power conversion circuit system," U.S. Patent 8,829,713, Sep. 9, 2014.

[23] P. Feuerstack, E. Weissenborn, and M. Kessler, "System for charging an energy store, and method for operating the charging system," U.S. Patent 9,312,692, Apr. 12, 2016.

[24] T. Takahara, S. Murakami, R. Kondo, and M. Yamada, "Power conversion device including a transformer with three or more windings," U.S. Patent 9,806,625, Oct. 31, 2017.

[25] S. Götz, "Device and method for integrating an electrical element into an electrical circuit under load," U.S. Patent 10,014,611, Jul. 3, 2018.

[26] M. Simon and M. Thurmeier, "Battery for a motor vehicle and motor vehicle," U.S. Patent 11,196,124, Dec. 7, 2021.

[27] S. Ci, N. Lin, and D. Wu, "Reconfigurable battery techniques and systems: A survey," *IEEE Access*, vol. 4, pp. 1175–1189, 2016, doi: 10.1109/ACCESS.2016.2545338.

[28] Y. Ma, H. Lin, X. Wang, Z. Wang, and Z. Ze, "Analysis of battery fault tolerance in modular multilevel converter with integrated battery energy storage system," in *Proc. 20th Eur. Conf. Power Electron. Appl.*, Sep. 17–21, 2018, pp. 1–8.

[29] G. Liang, G. G. Farivar, G. N. B. Yadav, E. Rodriguez, and J. Pou, "Battery fault tolerance of modular multilevel converter-based battery energy storage systems with redundant submodules," in *Proc. IEEE 47th Annu. Conf. Ind. Electron. Soc.*, Oct. 13–16, 2021.

[30] G. Liang et al., "A comparison of the battery fault tolerance of modular multilevel converters with half-bridge and full-bridge submodules," in *Proc. IEEE Energy Convers. Congr. Expo.*, Oct. 10–14, 2021, pp. 153–159.

[31] S. Ali, Z. Ling, K. Tian, and Z. Huang, "Recent advancements in submodule topologies and applications of MMC," *IEEE J. Emerg. Sel. Topics Power Electron.*, vol. 9, no. 3, pp. 3407–3435, Jun. 2021, doi: 10.1109/JESTPE.2020.2990689.

[32] T. Zheng et al., "A novel Z-type modular multilevel converter with capacitor voltage self-balancing for grid-tied applications," *IEEE Trans. Power Electron.*, vol. 36, no. 2, pp. 1399–1411, Feb. 2021, doi: 10.1109/TPEL.2020.2997991.

[33] S. Xu, "A new multilevel AC/DC topology based H-bridge alternate arm converter," *IEEE Access,* vol. 8, pp. 57997–58005, 2020, doi: 10.1109/ACCESS.2020.2982202.

[34] N. Tashakor, J. Kacetl, D. Keshavarzi, and S. Goetz, "Topology, analysis, and modulation strategy of a fully controlled modular reconfigurable battery pack with interconnected output ports for electric vehicles," *IEEE Trans. Transp. Electrific.*, to be published, doi: 10.1109/TTE.2023.3263775.

[35] M. Quraan, P. Tricoli, S. D'Arco, and L. Piegari, "Efficiency assessment of modular multilevel converters for battery electric vehicles," *IEEE Trans. Power Electron.*, vol. 32, no. 3, pp. 2041–2051, Mar. 2017.

[36] N. Tashakor, B. Arabsalmanabadi, L. O. Cervera, E. Hosseini, K. Al-Haddad, and S. Goetz, "A simplified analysis of equivalent resistance in modular multilevel converters with parallel functionality," in *Proc. 46th Annu. Conf. IEEE Ind. Electron. Soc.*, Oct. 18–21, 2020, pp. 4158–4163.

[37] K. Ilves, L. Bessegato, L. Harnefors, S. Norrga, and H.-P. Nee, "Semi-full-bridge submodule for modular multilevel converters," in *Proc. 9th Int. Conf. Power Electron. ECCE Asia*, 2015, pp. 1067–1074.

[38] J. Xu, J. Li, J. Zhang, L. Shi, X. Jia, and C. Zhao, "Open-loop voltage balancing algorithm for two-port full-bridge MMC-HVDC system," *Int. J. Elect. Power Energy Syst.*, vol. 109, pp. 259–268, 2019, doi: 10.1016/j.ijepes.2019.01.032.

[39] Z. Li, R. Lizana, A. V. Peterchev, and S. M. Goetz, "Distributed balancing control for modular multilevel series/parallel converter with capability of sensorless operation," in *Proc. IEEE Energy Convers. Congr. Expo.*, 2017, pp. 1787–1793.

[40] N. Tashakor, J. Kacetl, T. Kacetl, and S. Goetz, "Modular battery-integrated power electronics-modelling, advantages, and challenges," in *Proc. 24th Eur. Conf. Power Electron. Appl.*, 2022, pp. 1–10.

[41] Z. Ma et al., "Multilayer SOH equalization scheme for MMC battery energy storage system," *IEEE Trans. Power Electron.*, vol. 35, no. 12, pp. 13514–13527, Dec. 2020, doi: 10.1109/TPEL.2020.2991879.

[42] Z. Ma, F. Gao, C. Zhang, W. Li, and D. Niu, "Variable DC-link voltage regulation of single-phase MMC battery energy-storage system for reducing additional charge throughput," *IEEE Trans. Power Electron.*, vol. 36, no. 12, pp. 14267–14281, Dec. 2021, doi: 10.1109/TPEL.2021.3084605.

[43] J. G. Pinto, V. Monteiro, H. Goncalves, and J. L. Afonso, "Onboard reconfigurable battery charger for electric vehicles with traction-to-auxiliary mode," *IEEE Trans. Veh. Technol.*, vol. 63, no. 3, pp. 1104–1116, Mar. 2014, doi: 10.1109/TVT.2013.2283531.

[44] A. M. Naradhipa, S. Kim, D. Yang, S. Choi, I. Yeo, and Y. Lee, "Power density optimization of 700kHz GaN-based auxiliary power module for electric vehicles," *IEEE Trans. Power Electron.*, vol. 36, no. 5, pp. 5610–5621, May 2021, doi: 10.1109/TPEL.2020.3026328.

[45] K. Kandasamy, D. M. Vilathgamuwa, U. K. Madawala, and K. Tseng, "Inductively coupled modular battery system for electric vehicles," *IET Power Electron.,* vol. 9, no. 3, pp. 600–609, 2016, doi: 10.1049/iet-pel.2014.0553.

[46] M. M. U. Rehman, F. Zhang, M. Evzelman, R. Zane, and D. Maksimovic, "Control of a series-input, parallel-output cell balancing system for electric vehicle battery packs," in *Proc. IEEE 16th Workshop Control Model. Power Electron.*, Jul. 12–15, 2015, pp. 1–7.

[47] M. M. U. Rehman et al., "Modular approach for continuous cell-level balancing to improve performance of large battery packs," in *Proc. IEEE Energy Convers. Congr. Expo.*, Sep. 14–18, 2014, pp. 4327–4334.

[48] C. Li, W. Huang, R. Cao, F. Bu, and C. Fan, "An integrated topology of charger and drive for electric buses," *IEEE Trans. Veh. Technol.*, vol. 65, no. 6, pp. 4471–4479, Jun. 2016, doi: 10.1109/TVT.2016.2519943.

[49] A. K. Bhattacharjee, N. Kutkut, and I. Batarseh, "Review of multiport converters for solar and energy storage integration," *IEEE Trans. Power Electron.*, vol. 34, no. 2, pp. 1431–1445, Feb. 2019, doi: 10.1109/TPEL.2018.2830788.

[50] M. Vasiladiotis and A. Rufer, "A modular multiport power electronic transformer with integrated split battery energy storage for versatile ultrafast EV charging stations," *IEEE Trans. Ind. Electron.*, vol. 62, no. 5, pp. 3213–3222, May 2015, doi: 10.1109/TIE.2014.2367237.

[51] F. Chen, W. Qiao, and L. Qu, "A modular and reconfigurable battery system," in *Proc. IEEE Appl. Power Electron. Conf. Expo.*, Mar. 26–30, 2017, pp. 2131–2135.

[52] Z. Li, R. Lizana, S. Sha, Z. Yu, A. V. Peterchev, and S. Goetz, "Module implementation and modulation strategy for sensorless balancing in modular multilevel converters," *IEEE Trans. Power Electron.*, vol. 34, no. 9, pp. 8405–8416, Sep. 2019.

[53] J. Fang, F. Blaabjerg, S. Liu, and S. M. Goetz, "A review of multilevel converters with parallel connectivity," *IEEE Trans. Power Electron.*, vol. 36, no. 11, pp. 12468–12489, Nov. 2021, doi: 10.1109/TPEL.2021.3075211.

[54] S. Gonzalez, S. Verne, and M. Valla, *Multilevel Converters for Industrial Applications*, Boca Raton, FL, USA: CRC, 2014, doi: 10.1201/b15252.

[55] D. Ronanki and S. S. Williamson, "Modular multilevel converters for transportation electrification: Challenges and opportunities," *IEEE Trans. Transp. Electrific.,* vol. 4, no. 2, pp. 399–407, Jun. 2018.

[56] N. Tashakor, Z. Li, and S. M. Goetz, "A generic scheduling algorithm for low-frequency switching in modular multilevel converters with parallel functionality," *IEEE Trans. Power Electron.*, vol. 36, no. 3, pp. 2852–2863, Mar. 2021, doi: 10.1109/TPEL.2020.3018168.

[57] Z. Li, J. K. Motwani, Z. Zeng, S. Lukic, A. V. Peterchev, and S. Goetz, "A reduced series/parallel module for cascade multilevel static compensators supporting sensorless balancing," *IEEE Trans. Ind. Electron.*, vol. 68, no. 1, pp. 15–24, Jan. 2021, doi: 10.1109/TIE.2020.2965470.

[58] J. Fang, Z. Li, and S. Goetz, "Multilevel converters with symmetrical half-bridge submodules and sensorless voltage balance," *IEEE Trans. Power Electron.*, vol. 36, no. 1, pp. 447–458, Jan. 2021, doi: 10.1109/TPEL.2020.3000469.

[59] M. Khayamy and H. Chaoui, "Efficient PMSM-inverter-based drive for vehicular transportation systems," *IEEE Trans. Veh. Technol.,* vol. 67, no. 6, pp. 4783–4792, Jun. 2018, doi: 10.1109/TVT.2018.2798359.

[60] J. O. Estima and A. J. M. Cardoso, "Efficiency analysis of drive train topologies applied to electric/hybrid vehicles," *IEEE Trans. Veh. Technol.,* vol. 61, no. 3, pp. 1021–1031, Mar. 2012, doi: 10.1109/TVT.2012.2186993.

[61] S. Xiao, X. Gu, Z. Wang, T. Shi, and C. Xia, "A novel variable DC-link voltage control method for PMSM driven by a quasi-Z-source inverter," *IEEE Trans. Power Electron.,* vol. 35, no. 4, pp. 3878–3890, Apr. 2020, doi: 10.1109/TPEL.2019.2936267.

[62] A. Mahmoudi, W. L. Soong, G. Pellegrino, and E. Armando, "Loss function modeling of efficiency maps of electrical machines," *IEEE Trans. Ind. Appl.,* vol. 53, no. 5, pp. 4221–4231, Sep./Oct. 2017.

[63] K. Gökce and A. Ozdemir, "An instantaneous optimization strategy based on efficiency maps for internal combustion engine/battery hybrid vehicles," *Energy Convers. Manage.*, vol. 81, pp. 255–269, 2014.

[64] N. Tashakor, M. Kilictas, E. Bagheri, and S. Goetz, "Modular multilevel converter with sensorless diode-clamped balancing through level-adjusted phase-shifted modulation," *IEEE Trans. Power Electron.*, vol. 36, no. 7, pp. 7725–7735, Jul. 2021, doi: 10.1109/TPEL.2020.3041599.

[65] N. Li, F. Gao, T. Hao, Z. Ma, and C. Zhang, "SOH balancing control method for the MMC battery energy storage system," *IEEE Trans. Ind. Electron.,* vol. 65, no. 8, pp. 6581–6591, Aug. 2018, doi: 10.1109/TIE.2017.2733462.

[66] S. Chowdhury, M. N. B. Shaheed, and Y. Sozer, "State-of-charge balancing control for modular battery system with output DC bus regulation," *IEEE Trans. Transp. Electrific.,* vol. 7, no. 4, pp. 2181–2193, Dec. 2021, doi: 10.1109/TTE.2021.3090735.

[67] J. Kacetl, J. Fang, T. Kacetl, N. Tashakor, and S. Goetz, "Design and analysis of modular multilevel reconfigurable battery converters for variable bus voltage powertrains," *IEEE Trans. Power Electron.*, vol. 38, no. 1, pp. 130–142, Jan. 2023, doi: 10.1109/TPEL.2022.3179285.

[68] D. Kraus, E. Specht, T. Merz, and M. Hiller, "Optimized real-time control for modular multilevel converters using adaptive neural networks," in *Proc. 21st Eur. Conf. Power Electron. Appl.*, 2019, pp. P.1–P.8, doi: 10.23919/EPE.2019.8915464.

[69] M. Gjelaj, S. Hashemi, C. Traeholt, and P. B. Andersen, "Grid integration of DC fast-charging stations for evs by using modular li-ion batteries," *IET Gener., Transmiss. Distrib.,* vol. 12, no. 20, pp. 4368–4376, 2018, doi: 10.1049/iet-gtd.2017.1917.

[70] M. Quraan, T. Yeo, and P. Tricoli, "Design and control of modular multilevel converters for battery electric vehicles," *IEEE Trans. Power Electron.,* vol. 31, no. 1, pp. 507–517, Jan. 2016, doi: 10.1109/TPEL.2015.2408435.

[71] N. Tashakor, B. Arabsalmanabadi, F. Naseri, and S. Goetz, "Low-cost parameter estimation approach for modular converters and reconfigurable battery systems using dual-Kalman-filter," *IEEE Trans. Power Electron.*, vol. 37, no. 6, pp. 6323–6334, Jun. 2022, doi: 10.1109/TPEL.2021.3137879.